



1 **Transition from hydrothermal vents to cold seeps records timing of**
2 **carbon release in the Guaymas Basin, Gulf of California**

3 Sonja Geilert¹, Christian Hensen¹, Mark Schmidt¹, Volker Liebetrau¹, Florian Scholz¹,
4 Mechthild Doll², Longhui Deng³, Mark A. Lever³, Chih-Chieh Su⁴, Stefan Schlömer⁵, Sudipta
5 Sarkar⁶, Volker Thiel⁷, Christian Berndt¹

6

7 ¹GEOMAR Helmholtz Centre for Ocean Research Kiel, Wischhofstraße 1-3, 24148 Kiel, Germany

8 ²Universität Bremen, Klagenfurter-Straße 4, 28359 Bremen, Germany

9 ³ Department of Environmental Systems Science, ETH Zurich, Universitätstrasse 16, 8092 Zurich,
10 Switzerland

11 ⁴Institute of Oceanography, National Taiwan University, No. 1, Sec. 4, Roosevelt Road, Taipei 106,
12 Taiwan

13 ⁵Federal Institute for Geosciences and Natural Resources, Stilleweg 2, 30655 Hannover, Germany

14 ⁶Department of Earth and Climate Science, Indian Institute of Science Education and Research Pune,
15 Dr. Homi Bhabha Road, Maharashtra-411008, India

16 ⁷Geobiology, Geoscience Centre, Georg-August University Göttingen, Goldschmidtstr. 3, 37077
17 Göttingen, Germany

18

19 **Abstract**

20

21 The Guaymas Basin in the Gulf of California is an ideal site to test the hypothesis that
22 magmatic intrusions into organic-rich sediments can cause the release of large amounts of
23 thermogenic methane and CO₂ that may lead to climate warming. In this study pore fluids
24 close (~500 m) to a hydrothermal vent field and at cold seeps up to 20 km away from the
25 northern rift axis were studied to determine the influence of magmatic intrusions on pore
26 fluid composition and gas migration. Pore fluids close to the hydrothermal vent area show
27 predominantly seawater composition, indicating a shallow circulation system transporting
28 seawater to the hydrothermal catchment area rather than being influenced by hydrothermal
29 fluids themselves. Only in the deeper part of the sediment core, composed of hydrothermal
30 vent debris, Sr isotopes indicate a mixture with hydrothermal fluids of ~3%. Also cold seep
31 pore fluids show mainly seawater composition. Most of the methane is of microbial origin
32 and consumed by anaerobic oxidation in shallow sediments, whereas ethane has a clear
33 thermogenic signature. Fluid and gas flow might have been active during sill emplacement in
34 the Guaymas Basin, but ceased 28 to 7 thousand years ago, based on sediment thickness
35 above extinct conduits. Our results indicate that carbon release depends on the longevity of
36 sill-induced, hydrothermal systems which is a currently unconstrained factor.



37

38 **1 Introduction**

39

40 Climate change events in Earth's history have been partly related to the injection of large
41 amounts of greenhouse gases into the atmosphere (e.g. Svensen et al., 2004; Gutjahr et al.,
42 2017). One of the most prominent events was the Paleocene-Eocene Thermal Maximum
43 (PETM) during which the Earth's atmosphere warmed by about 8°C in less than 10,000 years
44 (Zachos et al., 2003). The PETM was possibly triggered by the emission of about 2000 Gt of
45 carbon (Dickens, 2003; Zachos et al., 2003). Processes discussed to release these large
46 amounts of carbon in a relatively short time are gas hydrate dissociation and igneous
47 intrusions into organic-rich sediments, triggering the release of carbon during contact
48 metamorphism (Kennett et al., 2000; Svensen et al., 2004). The Guaymas Basin in the Gulf of
49 California is considered one of the few key sites to study carbon release in a rift basin
50 exposed to high sedimentation rates.

51 The Gulf of California is located between the Mexican mainland and the Baja California
52 Peninsula, north of the East Pacific Rise (EPR; Fig. 1). The spreading regime at EPR continues
53 into the Gulf of California and changes from a mature, open ocean-type to an early-opening
54 continental rifting environment with spreading rates of about 6 cm yr⁻¹ (Curry & Moore,
55 1982). The Guaymas Basin, which is about 240 km long, 60 km wide, and reaching water
56 depths of up to 2000 m, is known as a region of vigorous hydrothermal activity (e.g. Curry
57 and Moore, 1982; Gieskes et al., 1982; Von Damm et al., 1985). Its spreading axis consists of
58 two graben systems (northern and southern troughs) offset by a transform fault (Fig. 1). In
59 contrast to open ocean spreading centres like the EPR, the rifting environment in the
60 Guaymas Basin shows a high sediment accumulation rate of up to 0.8-2.5 m kyr⁻¹ resulting in
61 organic-rich sedimentary deposits of several hundreds of meters in thickness (e.g. Calvert,
62 1966; DeMaster, 1981; Berndt et al., 2016). The high sedimentation rate is caused by high
63 biological productivity in the water column and influx of terrigenous matter from the
64 Mexican mainland (Calvert, 1966).

65 Hydrothermal activity in the Guaymas Basin was first reported in the southern trough (e.g.
66 Lupton, 1979; Gieskes et al., 1982; Campbell and Gieskes, 1984; Von Damm et al., 1985).
67 Here, fluids emanate, partly from Black Smoker type vents at temperatures of up to 315°C



68 (Von Damm et al., 1985). Sills and dikes intruding into the sediment cover significantly affect
69 temperature distribution, and hence environmental conditions (Biddle et al., 2012; Einsele et
70 al., 1980; Kastner, 1982; Kastner and Siever, 1983; Simoneit et al., 1992; Lizarralde et al.,
71 2010; Teske et al., 2014). The magmatic intrusions accelerate early-diagenetic processes and
72 strongly influence the chemistry of the interstitial waters (e.g. Gieskes et al., 1982; Brumsack
73 and Gieskes, 1983; Kastner and Siever, 1983; Von Damm et al., 1985). Lizarralde et al. (2010)
74 reported that sills intruded into the sediment cover and that cold seeps at the seafloor are
75 visible up to 50 km away from the rift axis. They proposed a recently active magmatic
76 process that released much higher amounts of carbon into the water column than previously
77 thought. It was assumed that magmatic intrusions trigger the alteration of organic-rich
78 sediments and release thermogenic methane and CO₂. Varying methane concentrations and
79 temperature anomalies in the water column were interpreted as active thermogenic
80 methane production generated by contact metamorphism (Lizarralde et al., 2010). This
81 process might cause a maximum carbon flux of 240 kt C yr⁻¹ and might induce profound
82 climatic changes.

83 During the SO241 expedition in June/ July 2015 a new hydrothermal vent field was
84 discovered at the flank of the northern trough (Fig. 1; Berndt et al., 2016). The discovered
85 mound rises up to 100 m above the seafloor and predominantly Black Smoker type vents
86 suggest similar endmember temperatures and geochemical composition as found at the
87 southern trough (Berndt et al., 2016; von Damm et al. 1985). Berndt et al. (2016) discovered
88 an active hydrothermal vent system comprised of black smoker-type chimneys that release
89 methane-rich fluids with a helium isotope signature indicative of mid-ocean ridge basalt. The
90 vigorous release of large amounts of methane and CO₂ several hundred of meters into the
91 water column combined with magmatic intrusions into underlying sediments led Berndt et
92 al. (2016) to support the hypothesis that this process might have triggered the PETM during
93 opening of the North Atlantic as proposed by Svensen et al. (2004).

94 During RV SONNE cruise SO241, both, the recently discovered hydrothermal vent in the
95 northern trough (Berndt et al., 2016) and some of the off-axis seeps (Lizarralde et al. 2010)
96 which are located above potential sill intrusions were investigated by sediment, carbonate,
97 and water column sampling. Here, we present fluid and gas geochemical data from both



98 systems as well as carbonate data and discuss these data in the context of seismic data in
99 order to constrain subsurface processes and fluid origin.

100

101 **2 Materials and methods**

102 2.1 Sampling devices and strategy

103

104 During the RV SONNE expedition SO241 seven sites across the central graben of the
105 Guaymas basin were investigated (Fig. 1). Site-specific sampling and data recording was
106 performed using a (1) video-guided multicorer (MUC), (2) gravity corer (GC), (3) temperature
107 loggers attached to the GC or sediment probe, (5) CTD / Rosette water sampler, and (6)
108 video-guided hydraulic grab (VgHG). Sites were selected according to published data on the
109 location of seeps (Lizarralde et al., 2010) and seismic data acquired during the cruise (see
110 below).

111

112 2.1.1 Seismic data recording

113

114 Seismic data were collected using a Geometrics GeoEel Streamer of 150 to 183.5 m length
115 and 96 and 112 channels, respectively. Two GI guns in harmonic mode (105/105 cubic inch)
116 served as the seismic source. Processing included navigation processing (1.5625 m crooked
117 line binning), 20, 45, 250, 400 Hz frequency filtering, and poststack Stolt migration with
118 water velocity yielding approximately 2 m horizontal and 5 m vertical resolution close to the
119 seafloor.

120

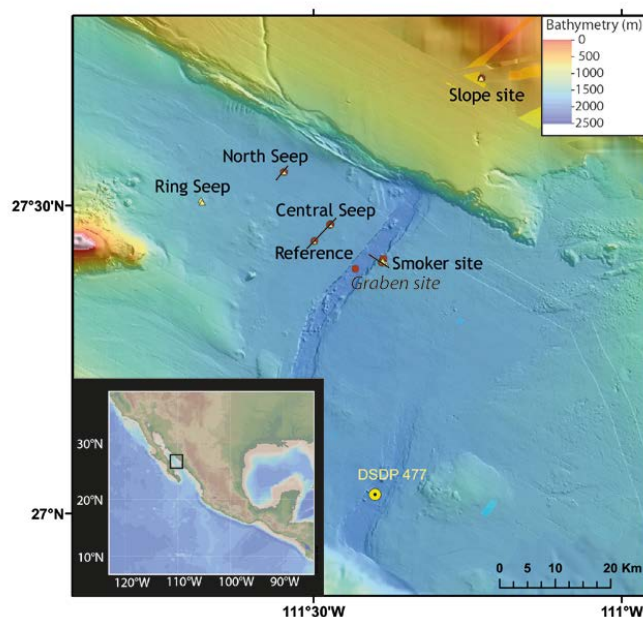
121 2.1.2 Sediment and pore fluid sampling

122

123 At seepage and vent sites, the video-guided multicorer was used to discover recent fluid
124 release, which is indicated by typical chemosynthetic biological communities at the seafloor
125 (bacterial mats, bivalves, etc.). However, small-scale, patchy distributions of active seepage
126 spots and visibility of authigenic concretions made it difficult to select the “best possible”
127 sampling locations for getting fine-grained sediment samples. Hence, comparing results from
128 different seeps might be biased in this regard. GC deployments were typically performed at



129 pre-inspected MUC sites or at the center of suspected seeps (based on bathymetry and
130 seismic data).
131 In total, we present pore fluid data collected at three seepage sites, North (GC01, MUC11),
132 Central (GC03, GC13, GC15, MUC04), and Ring Seeps (MUC05), one Reference Site (no active
133 seep site, see definition above; GC04, MUC02), and one active hydrothermal site, Smoker
134 (GC09, GC10, MUC15, MUC16). A Reference Site, that did not show active seepage or faults
135 indicated by seismic data, was chosen to obtain geochemical background values. In addition,
136 the slope towards the Mexican mainland was sampled as well (GC07) (Fig. 1, Table 1). After
137 core retrieval, gravity cores were cut and split on deck and immediately sampled. Samples
138 were transferred into a cooling lab at 4°C and processed within 1 or 2 hours. Pore fluids were
139 obtained by pressure filtration. Sediment samples for hydrocarbon gases were taken on deck
140 with syringes and transferred to vials containing concentrated NaCl solution (after Sommer
141 et al., 2009). After multicorer retrieval, bottom water was sampled and immediately filtered
142 for further analyses. The sediment was transferred into a cooling lab and sampling was
143 executed in an argon-flushed glove bag. Pore fluids were retrieved by centrifugation and
144 subsequent filtration using 0.2 µm cellulose acetate membrane filters.



145



146 Figure 1: Sample locations in the Guaymas Basin, Gulf of California, during RV SONNE
147 expedition SO241. Black lines refer to seismic profiles, displayed in Fig. 2. Graben Site refers
148 to water column sampling only.

149

150 2.1.3 Subseafloor temperature measurements

151

152 Temperature gradients and thermal conductivity were measured at North Seep, Central
153 Seep, Reference Site, and Smoker Site as well as along a transect across the newly
154 discovered hydrothermal vent field and the rift valley. Miniaturized temperature loggers
155 (MTL) were attached to gravity cores or to a 5 m long sediment lance at a sampling rate of 1
156 s. The absolute accuracy of these temperature measurements is about 0.1 K and the
157 temperature resolution is 0.001 K (Pfender and Villinger, 2002).

158 Thermal conductivity was measured on recovered core material in close vicinity to the MTLs
159 using the KD2 Pro Needle Probe instrument. For temperature measurements obtained by a
160 lance, a constant thermal conductivity of 0.7 W/m K was assumed. Data processing was
161 done according to Hartmann and Villinger (2002).

162

163 2.1.4 Water column sampling

164

165 Water samples were taken by using a video-guided Niskin Water sampler Rosette System
166 (Schmidt et al., 2015) in order to study water column chemistry (i.e. dissolved CH₄) and
167 oceanographic parameters (i.e. temperature, salinity, turbidity). Eight water sampling
168 locations were chosen in the vicinity of MUC and GC stations and are termed North
169 (VCTD03), Central (VCTD02), Ring (VCTD01), Graben (CTD01; no video-guided sampling),
170 Smoker (VCTD06 and 10), and Slope (VCTD07). Additionally, hydrocarbon data published in
171 Berndt et al. (2016) from the Smoker Site (VCTD09) are shown. The (V)CTDs were either used
172 in a towed mode (VCTD03, 06, 09, 10) or in station (CTD01; VCTD01, 02, 07) keeping
173 hydrocast mode. The water depth was controlled based on pressure readings, altitude
174 sensors (<50 m distance to bottom), and online video observation (1 - 2 m above the
175 seafloor).

176

177 2.1.5 Authigenic carbonate sampling



178

179 At Central Seep a block (approx. 1 x 0.5 x 0.3 m) mainly consisting of solidified carbonate
180 matrix covered by a whitish carbonate rim and characterized by coarse open pore space in
181 mm to cm scale (see supplementary Fig. 1S) was recovered in 1843 m water depth from the
182 surface of a typical cold seep environment (close to high abundance of tube worms) by the
183 deployment of a video-guided hydraulic grab (VgHG, GEOMAR).

184

185 2.2 Sample treatment and analytical procedures

186

187 Pore fluids were analyzed onboard by photometry (hydrogen sulfide and NH_4) and titration
188 (total alkalinity = TA). Subsamples were analyzed in shore-based laboratories for major
189 anions and cations using ion chromatography (IC, METROHM 761 Compact, conductivity
190 mode) and inductively coupled plasma optical emission spectrometry (ICP-OES, VARIAN 720-
191 ES), respectively. Detailed descriptions can be found elsewhere (e.g. Scholz et al., 2013). All
192 chemical analyses were tested for accuracy and reproducibility using the IAPSO salinity
193 standard (Gieskes et al., 1991).

194 Strontium isotope ratios were analyzed by Thermal Ionization Mass Spectrometry (TIMS,
195 Triton, ThermoFisher Scientific). The samples were chemically separated via cation exchange
196 chromatography using the SrSpec resin (Eichrom). The isotope ratios were normalized to
197 NIST SRM 987 value of 0.710248 (Howarth and McArthur, 2004) which reached a precision
198 of ± 0.000015 (2 sd, $n = 12$).

199 Water samples taken from Niskin bottles were transferred into 100 ml glass vials with helium
200 headspace of 5 ml and poisoned with 50 μl of saturated mercury chloride solution.

201 Hydrocarbon composition of headspace gases was determined using a CE 8000 TOP gas
202 chromatograph equipped with a 30 m capillary column (Restek Q-PLOT, 0.32 mm) and a
203 flame ionization detector (FID). Replicate measurements yielded a precision of <3% (2 sd).

204 Stable carbon isotopes of methane were measured using a continuous flow isotope ratio
205 mass spectrometer (cf-IRMS). A Thermo TRACE gas chromatograph was used to separate the
206 light hydrocarbon gases by injecting up to 1 ml headspace gas on a ShinCarbon ST100/120
207 packed gas chromatography column. The separated gases were combusted and



208 corresponding $\delta^{13}\text{C}$ values were determined using a Thermo MAT53 mass spectrometer. The
209 reproducibility of $\delta^{13}\text{C}$ measurements was $\pm 0.3\text{‰}$ VPDB (2 sd).

210 Stable hydrogen isotope compositions of methane were analyzed by separating methane
211 from other gases by online gas chromatography (Thermo Trace GC; isotherm at 30°C; 30 m
212 RT-Q-Bond column, 0.25 mm ID, film thickness 8 μm). Prior to stable isotope analysis using a
213 coupled MAT 253 mass spectrometer (Thermo) methane-H was reduced to dihydrogen at
214 1420°C. Data are reported in per mil relative to Standard Mean Ocean Water (SMOW). The
215 precision of $\delta\text{D-CH}_4$ measurements was $\pm 3\text{‰}$ (2 sd).

216

217 ^{210}Pb (46.52 keV) and ^{214}Pb (351.99 keV) were simultaneously measured by two HPGe
218 gamma spectrometry systems (ORTEC GMX-120265 and GWL-100230), each interfaced to a
219 digital gamma-ray spectrometer (DSPECPlus™). Efficiency calibration of the gamma detectors
220 were calibrated using IAEA reference materials, coupled with an in-house secondary
221 standard for various masses (Huh et al., 2006; Lee et al., 2004). ^{214}Pb was used as an index of
222 ^{226}Ra (supported ^{210}Pb) whose activity concentration was subtracted from the total ^{210}Pb to
223 obtain excess ^{210}Pb ($^{210}\text{Pb}_{\text{ex}}$). The activities of radionuclides were decay-corrected to the date
224 of sample collection. All radionuclide data are calculated on salt-free dry weight basis.

225

226 A representative sample of the authigenic carbonate (cm-scale) was broken from the upper
227 surface of the block, gently cleaned from loosely bound sediment and organic remains and
228 dried at 20°C for 12 hrs. Two different subsamples were prepared by drilling material with a
229 handheld mm-sized mini-drill from the outer rim (whitish coating, lab code: 470-15) and the
230 related inner core (dark matrix, lab code: 472-15).

231 Prior to aliquot procedures both subsamples were finely ground in an agate mortar
232 providing homogeneous aliquots of suitable grain size for the combined approach of mineral
233 identification by X-ray diffractometry (XRD) (Philips X-ray diffractometer PW 1710 in
234 monochromatic $\text{CuK}\alpha$ mode between 2 and 70 2θ (incident angle), for details see
235 supplement), $\delta^{18}\text{O}$ and $\delta^{13}\text{C}$ analyses by stable isotope ratio mass spectrometry (SIRMS) and
236 U-Th geochronology by multi collector-inductively coupled plasma-mass spectrometry (MC-
237 ICP-MS) on a parallel leachate / sequential dissolution approach for single and isochron ages
238 (method see supplement) as well as $^{87}\text{Sr}/^{86}\text{Sr}$ isotope signatures for aliquots of the individual
239 U-Th solutions by thermal ionization mass spectrometry (TIMS, for method details please



240 refer to pore water Sr isotope analyses). Lipids extracts for biomarker determination were
241 analyzed as well (see below).

242

243 From each homogenized carbonate powder sample (see above), an aliquot of 10 mg was
244 separated for carbon $\delta^{13}\text{C}$ and oxygen $\delta^{18}\text{O}$ stable isotope analysis. A fraction from this
245 (approximately 1 mg) was dissolved by water-free phosphoric acid at 73°C in a “Carbo-Kiel”
246 (Thermo Fischer Scientific Inc.) online carbonate preparation line and measured for carbon
247 and oxygen stable isotope ratios with a MAT 253 mass spectrometer (Thermo-Fischer Inc.).
248 The $\delta^{13}\text{C}$ and $\delta^{18}\text{O}$ values are calculated as deviations from laboratory standard referred to
249 the PDB scale and reported in ‰ relative to V-PDB. The external reproducibility was checked
250 by replicate analyses of laboratory standards as being better than $\pm 0.04\text{‰}$ for $\delta^{13}\text{C}$ and
251 $\pm 0.1\text{‰}$ for $\delta^{18}\text{O}$ (1SD, n=7) for this sample set. However, the single measurement
252 uncertainties were significantly better and the resulting 2SD (n=3) for both main samples are
253 given in the supplement table S5.

254

255 Biomarkers were determined by grounding 4g of the sample and were then sequentially
256 extracted with dichloromethane (DCM)/methanol (3/1, v/v), DCM, and n-hexane
257 (ultrasonication, 20 min). The combined extracts were dried, derivatized using a
258 BSTFA/trimethylchlorosilane mixture (95/5, v/v; 1h; 40°C) and analysed by coupled gas
259 chromatography-mass spectrometry (GC-MS). GC-MS analyses were carried out with a
260 Thermo Fisher Trace 1310 GC coupled to a Quantum XLS Ultra MS. The GC was equipped
261 with a Phenomenex Zebron ZB 5MS capillary column (30 m, 0.1 μm film thickness, inner
262 diameter 0.25 mm). Fractions were injected splitless at 270°C. The carrier gas was He (1.5
263 mL/min). The GC oven temperature was ramped from 80°C (1 min) to 310°C at 5°C min⁻¹
264 and held for 20 min. Electron ionization mass spectra were recorded at 70 eV.

265

266 **3 Results**

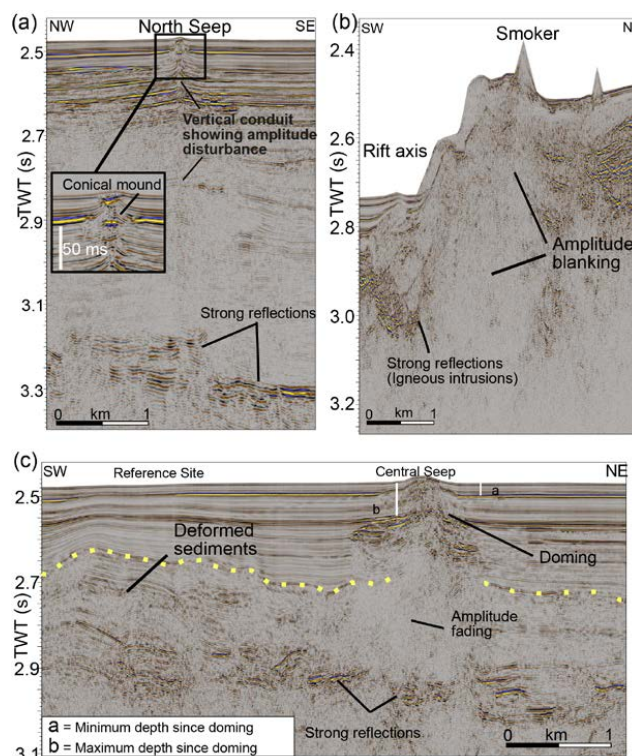
267 **3.1 Subsurface structure and evidence for sill-related fluid mobilization**

268

269 Seismic profiles show a wide range of sediment deformation (Fig. 2). Seismic amplitude
270 blanking along vertical zones below the seafloor indicates apparent fluid flow at North,
271 Central, and Ring Seep (Fig. 2). Underneath these locations, sediments are deformed.



272 Blankening of the seismic signal is attributed to sediment mobilization due to the
 273 hydrothermal activity in response to sill intrusion. In contrast, at the Reference Site
 274 sediments show a more or less continuous succession without vertical disturbance. At North
 275 Seep, a shallow high-amplitude reversed polarity reflector occurs at 50-60 mbsf. Sill depths
 276 are inferred from the seismic profiles at ~500 to 600 m for North Seep and with ~350 to 400
 277 mbsf at the other sites, assuming seismic interval velocities of 1600 to 2000 m s⁻¹. Seismic
 278 images suggest that massive disturbance of sediments and vertical pipe structures are
 279 related to channeled fluid and/or gas advection caused by sill intrusions (Fig. 2). Faults are
 280 indicated which may serve as fluid pathways above potential sill intrusions. Closer inspection
 281 of the seismic reflectors at the Central Seep (Fig 2c) shows onlap onto a doming structure.
 282 On the NW flank of the dome the deepest onlap occurs at 60 ms or 48 m below the sea floor
 283 (assuming 1600 m s⁻¹ sediment interval velocity) whereas on the SE flank the shallowest
 284 onlap occurs at 15 ms or 12 m below the sea floor.



285

286 Fig.2: Seismic profiles of North Seep (a), Smoker Site (b) as well as of Central Seep and
 287 Reference Site (c). Seismic section showing doming above the Central Seep. There are



288 different phases of onlap starting about 60 mbsf (maximum deposition) until about 15 mbsf
289 (minimum deposition) or 48 and 12 mbsf respectively assuming a sediment interval velocity
290 of 1600 m s^{-1} .

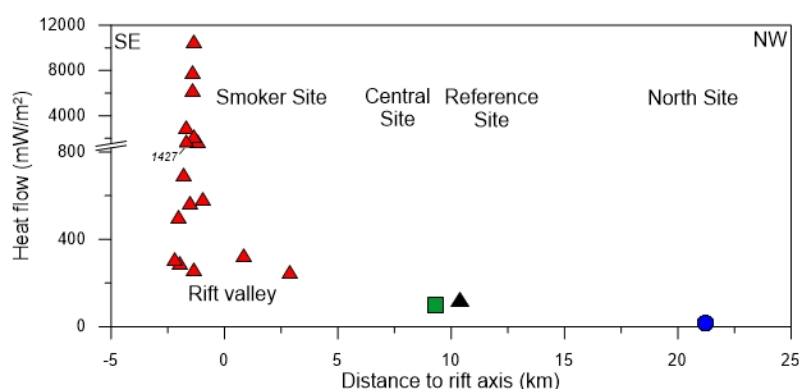
291

292 3.2 Temperature measurements

293

294 Heat flow and temperature gradients were measured at North and Central Seep, Reference
295 Site, and Smoker Site (attached to GCs) as well as in transects along the hydrothermal ridge
296 and rift axis (attached to a temperature lance; Fig. 3, Table 1). Highest heat flow values
297 occurred close to the Smoker Site and range between 599 and 10835 mW m^{-2} . Temperature
298 gradients were also highest at the Smoker Site ($\sim 15 \text{ K m}^{-1}$). In contrast, heat flow values and
299 temperature gradients in the rift valley close to the rift axis ranged between 262 and 338
300 mW m^{-2} and 0.4 to 0.5 K m^{-1} , respectively. Generally heat flow values decreased with
301 increasing distance to the rift axis with 140 mW m^{-2} at the Reference Site, 113 mW m^{-2} at
302 Central Seep, and 28 mW m^{-2} at North Seep. Temperature gradients are 0.22 K m^{-1} at the
303 Reference Site, 0.16 K m^{-1} at Central Site and 0.14 K m^{-1} at North Site.

304



305

306 Figure 3: Heat flow in the Guaymas Basin in relative distance to the rift axis.

307

308 3.3 Sediment characteristics and sedimentation rates

309

310 The sediments are mainly composed of organic-rich diatomaceous clay, consistent with
311 earlier analyses (e.g. Kastner, 1982). At North Seep, the sediments are composed of
312 homogeneous diatomaceous clay. Rare shell fragments and carbonate concretions are



313 present. Gas hydrates were discovered at 2.5 meters below seafloor (mbsf). Authigenic
314 carbonates were present at the seafloor. At Ring Seep, SW of North Seep, sediments are
315 predominantly composed of diatomaceous clay. At Central Seep, located between North
316 Seep and Smoker Site, sediments are composed of homogeneous diatomaceous clay
317 intercalated with shell fragments and banding of whitish layers in the lower meter of the GC.
318 At the seafloor, authigenic carbonates were present as well. At Smoker Site, ca. 500 m SE of
319 the hydrothermal vent field, surface sediments are likewise composed of diatomaceous clay
320 with light and dark greyish banding. Traces of bioturbation are visible in the upper 4 m.
321 Below about 4 m depth, a sharp contact defines the transition to hydrothermal deposits,
322 which are composed of mm-to-cm sized black to grey Fe-rich sulfides (for a detailed
323 description see Berndt et al. (2016)). Within the hydrothermal deposits brownish to grey clay
324 lenses appear. At the Slope Site, sediments are laminated in the mm- to cm-range. The
325 sediment is dominated by diatomaceous clay and only a few ash lenses exist.

326 The sedimentation rates ranged between 0.4 m kyr^{-1} at Smoker Site and 3.5 m kyr^{-1} at North
327 seep based on radionuclides measurements (Table 1). Sedimentation rates at all other sites
328 are about 2 m kyr^{-1} .

329

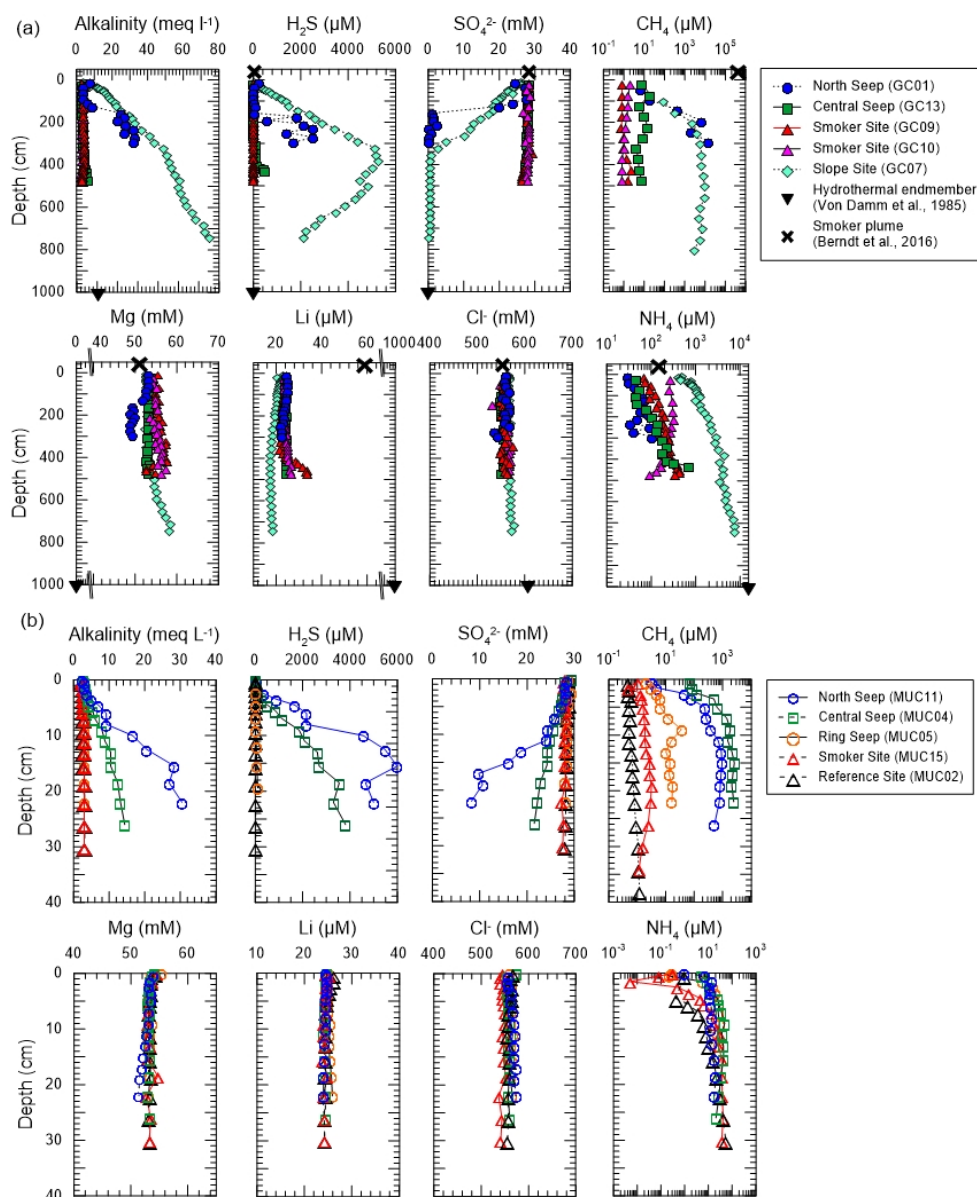
330 3.4 Pore water geochemistry

331

332 All pore water data and isotope measurements of $^{87}\text{Sr}/^{86}\text{Sr}$ are listed in supplementary table
333 S2. Pore water profiles of alkalinity, H_2S , SO_4^{2-} , CH_4 , NH_4 , Cl^- , Mg, and Li are shown in Fig. 4a
334 (GCs) and 4b (MUCs).

335

336



337

338

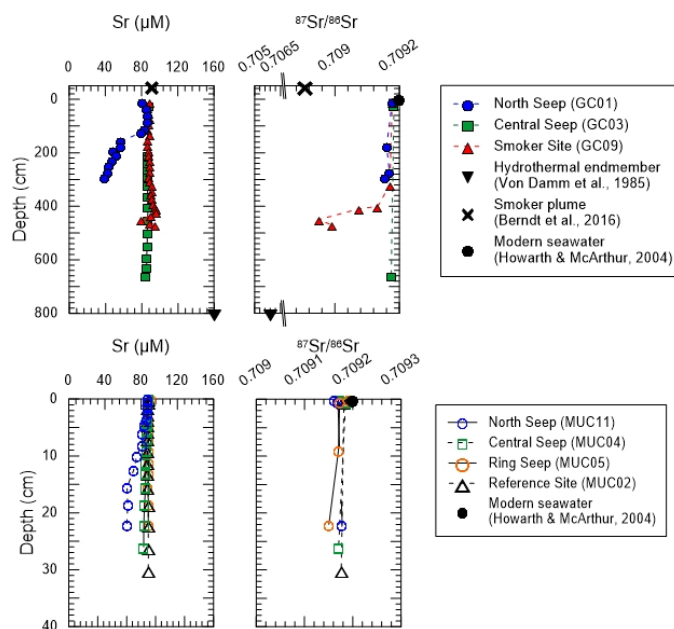
339 Figure 4: Pore water profiles of GCs (a) and MUCs (b). Endmember composition of
340 hydrothermal solutions from Von Damm et al. (1985) and hydrothermal plume geochemical
341 composition from Berndt et al. (2016) are shown as well in (a).

342



343 Pore water constituents plotted in Figure 4 were selected to characterize variations in
 344 organic matter diagenesis, anaerobic oxidation of methane (AOM), as well as potential
 345 water-rock interactions related to subsurface hydrothermal activity. In general, methane
 346 concentrations are elevated at the seep locations and at the slope, thus enhancing AOM.
 347 Alkalinity and H₂S increase with depth for North Seep, Central Seep, and Slope Site, while
 348 SO₄²⁻ is decreasing. AOM depths can only be inferred for North Seep with ~160cm and Slope
 349 Site with ~300cm. NH₄ is only slightly increasing with depth; higher NH₄-levels are only found
 350 at the Slope Site (Fig. 4). Concentrations of Cl⁻, Mg, and Li do not show significant variations
 351 from seawater.

352 Sr concentrations and isotopes are plotted in Fig. 5. Sr concentrations show predominantly
 353 modern seawater values, except at North Seep where they strongly decrease. The ⁸⁷Sr/⁸⁶Sr
 354 isotope ratios also show predominantly seawater values (0.709176; Howarth and McArthur,
 355 2004). North and Ring Seeps show slight decreases in ⁸⁷Sr/⁸⁶Sr, whereas values at the
 356 Smoker Site decrease strongly below the transition between hemipelagic sediments and
 357 hydrothermal deposits (Fig. 5). The ratios show a similar depletion as those from the
 358 hydrothermal plume (Berndt et al., 2016).



359



360 **Fig. 5.** Sr concentrations and $^{87}\text{Sr}/^{86}\text{Sr}$ ratios for GCs (upper panels) and MUCs (lower panels).
361 For comparison, data from the hydrothermal smoker plume (Berndt et al., 2016), the
362 hydrothermal endmember (Von Damm et al., 1985), and modern seawater (Howarth and
363 McArthur, 2004) are shown in the upper panel. Note the different scale for MUC $^{87}\text{Sr}/^{86}\text{Sr}$
364 ratios.

365

366 3.5 Pore water hydrocarbon gases, carbon and hydrogen isotope data

367

368 Concentrations of dissolved hydrocarbons and $\delta^{13}\text{C}_{\text{CH}_4}$, $\delta^{13}\text{C}_{\text{C}_2\text{H}_6}$, and $\delta\text{D}_{\text{CH}_4}$ data are reported
369 in supplementary table S3. Overall, our data show a large variability in $\text{CH}_4/(\text{C}_2\text{H}_6+\text{C}_3\text{H}_8)$ with
370 ratios between 100 and 10,000 and $\delta^{13}\text{C}_{\text{CH}_4}$ between -25 and -90 ‰. The $\delta^{13}\text{C}_{\text{C}_2\text{H}_6}$ values
371 range between -26.1 and -38.3 ‰ for North Seep and -29.6 and -37.7 ‰ for Central Seep.
372 The $\delta\text{D}_{\text{CH}_4}$ values at both seeps range between -97 and -196 ‰, for Slope Site between -192
373 and -196 ‰, and for the Smoker hydrothermal plume between -98 and -113 ‰.

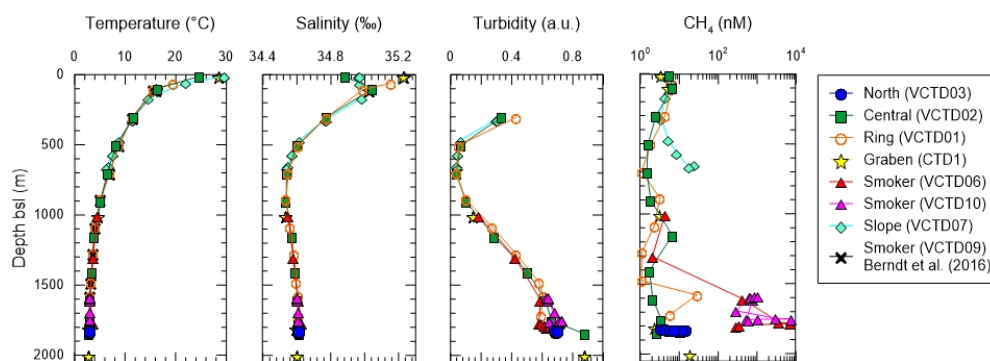
374

375 3.6 Water column data

376

377 Water column characteristics like temperature, salinity, turbidity as well as methane
378 concentrations are shown in figure 6 and supplementary table S4. Surface waters in the
379 Guaymas Basin show warm temperatures up to 29.5°C (salinity: 34.5‰) close to the Mexican
380 mainland (Slope, VCTD07) and up to 24.6°C (34.6‰) in the central basin (Central, VCTD02).
381 With depth, temperatures decrease continuously to 2.8 to 3.0°C (salinity: 34.6‰) close to
382 the sea floor (1600 - 1800m). Turbidity values are high in the deep water layer (~1400-
383 1800m) and indicate a well-mixed deep basin, also shown by relatively homogeneous
384 temperature and salinity data. Only the water column directly above the hydrothermal
385 smoker field (VCTD09) shows strongly elevated temperature (28.4°C) and salinity (35.1‰)
386 (Berndt et al., 2016). Methane concentrations are highest close to the smoker vent field (up
387 to 400 μM , (VCTD09; Berndt et al., 2016)), but still vary in the deep water column of the
388 basin between 2 and 28.1 nM (Central (VCTD02) and Ring (VCTD01), respectively).

389



390

391 Fig.6: Water column temperature, salinity, turbidity, and methane concentrations. Note that
392 the upper ~300m bsl in the turbidity data are not shown for scale matters. VCDT10
393 temperature data are from Berndt et al. (2016).

394

3.7 Authigenic carbonate data

395

396
397 The authigenic carbonate sample (Fig. S1) consists of 88 to 90 % aragonite and 6 to 12 %
398 calcite (supplementary Table S5). The bulk outer rim carbonate has an average carbon
399 isotope signature ($\delta^{13}\text{C}_{\text{V-PDB}}$) of $-46.6 \pm 0.2\text{‰}$ and an oxygen isotope signature ($\delta^{18}\text{O}_{\text{V-PDB}}$) of
400 $3.7 \pm 0.3\text{‰}$. Inner core carbonate isotope signatures yield similar values with $\delta^{13}\text{C}_{\text{V-PDB}}$ of -
401 $44.7 \pm 0.2\text{‰}$ and $\delta^{18}\text{O}_{\text{V-PDB}}$ of $3.6 \pm 0.1\text{‰}$ (Table S5). The average outer rim $^{87}\text{Sr}/^{86}\text{Sr}$ ratio is
402 0.709184 and the inner core ratio is 0.709176. External reproducibility of NIST-SRM987 is
403 0.000015 (2 SEM). The U-Th carbonate dating approach on these authigenic carbonates
404 implies formation ages younger than 240 yrs BP.

405 Lipids extracts obtained from seep carbonate 56-VgHG-4 (Central Site) revealed a strong
406 signal of specific prokaryote-derived biomarkers (Fig. S1). These compounds encompassed
407 archaeal isoprenoid lipids, namely crocetane, 2,6,10,15,19-pentamethylcosane(-icosenes
408 (PMI, PMI Δ) archaeol, and *sn*2-hydroxyarchaeol (see Fig. S1 for structures). In addition, the
409 sample contained a suite of non-isoprenoid 1,2-dialkylglycerolethers (DAGE) of bacterial
410 origin. Typical compounds of planktonic origin, such as sterols, were also present, but low in
411 abundance.

412

413



414 **4 Discussion**

415 4.2 Origin of seeping fluids

416 4.2.1 Black Smoker Site

417

418 The water column above the newly discovered vent exhibits elevated CH₄ concentrations (up
419 to 400 μM) and pCO₂ data (>6000 μatm), and the range of measured stable isotope
420 signature of methane (δ¹³C_{CH₄} between -39‰ and -14.9‰) and a Helium (³He) isotope
421 anomaly clearly indicates gas exhalations from thermogenic organic matter degradation with
422 contributions from a mantle source (Berndt et al., 2016). These northern trough
423 hydrothermal fluids are comparable in their gas geochemistry to the southern trough
424 (Lupton, 1979; Von Damm et al., 1985) as was demonstrated by endmember calculations in
425 Berndt et al., 2016. However, the highest heat flow values up to 10835 mW/m² are found
426 close to the Smoker Site and are much higher than observed in earlier studies in which
427 maximal 2000 mW/m² were measured in the center of the trough (Fisher and Becker, 1991).
428 The high heat flow at Smoker Site even exceeds the hydrothermally more active southern
429 trough where heat flow values of 2000 to 9000 mW/m² were measured (Fisher and Becker,
430 1991; Lonsdale and Becker, 1985). This might indicate that hydrothermal activity at the
431 northern trough is younger and a more recent process compared to the southern trough.

432 Despite the proximity of the gravity cores (GC09, GC10) and multicorer-cores (MUC15,
433 MUC16) to the hydrothermal vent field (~500m distance; temperatures measured
434 immediately after retrieval are up to 60°C) pore fluid geochemical signatures within nearby
435 sediments are not much different from those in seawater (Fig. 4). Specifically Mg, Li, Cl, and
436 ⁸⁷Sr/⁸⁶Sr which are considered as good indicators for hydrothermal alterations and/or deep-
437 seated diagenetic processes do not show any prominent excursions from seawater values.
438 Hydrothermal fluids are typically depleted in Mg and highly enriched in fluid-mobile
439 elements like Li caused by high-temperature reactions with mafic rocks (here sills) and/or
440 sediments through which they percolate (e.g. Einsele et al., 1980; Gieskes et al., 1982;
441 Kastner, 1982; Von Damm et al., 1985; Lizarralde et al., 2010; Teske et al., 2016). Such
442 compositions are reported from DSDP site 477 (Gieskes et al., 1982) and fluids obtained by
443 Alvin dives (Von Damm et al., 1985). Although strongly diluted, CTD samples from the Black
444 Smoker plume in the Northern trough show this trend (Berndt et al., 2016). Our data



445 therefore suggest that the sediments surrounding the Black Smoker area are not percolated
446 by hydrothermal fluids. We hypothesize that hydrothermal venting causes a shallow
447 convection cell (e.g. Henry et al., 1996) drawing seawater through the sediments towards
448 the smoker, while the sediments become heated by lateral heat conduction.

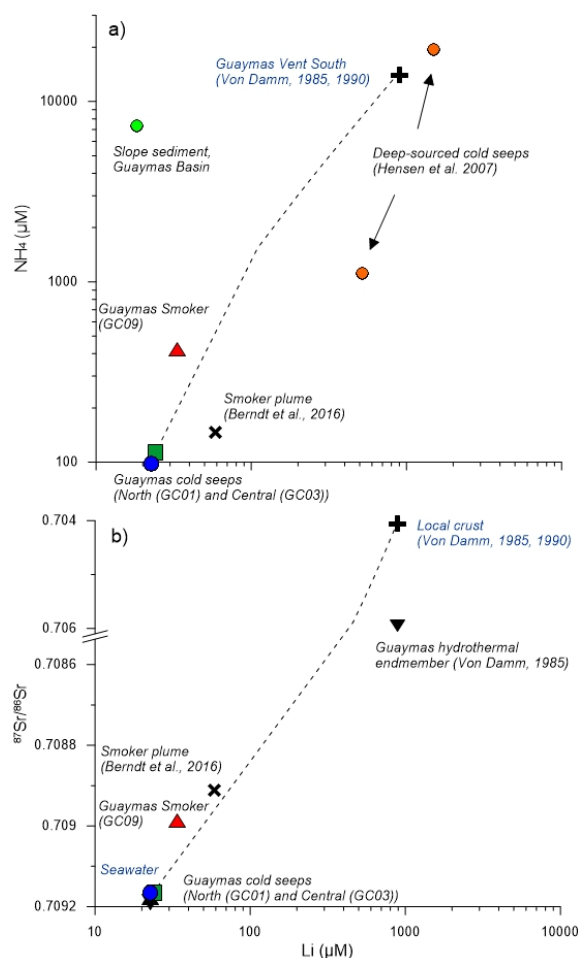
449 Geochemical indicators for a diagenetic or catagenetic breakdown of organic matter like NH_4
450 are only poorly enriched in sediments surrounding the black smoker vents. Expected end-
451 member values should be similar to those reported from the southern trough (20mM; Von
452 Damm et al. (1985)), but they remain well below ($\leq 0.3\text{mM}$). For comparison, intense organic
453 matter breakdown occurs in areas with high sediment accumulation rates like the
454 continental slope (Simoneit et al., 1986). Here, maximum NH_4 -levels of 1-10 mM
455 (accompanied by high levels of alkalinity and AOM; Fig. 3) are reached in the pore water
456 already at subsurface depths of only a few meters, confirming that a fluid mobilized from
457 greater subsurface depth must be enriched in NH_4 and other products of organic matter
458 degradation. Overall, this confirms that early-diagenetic processes are not intense around
459 the Smoker Mound and further indicates a shallow convection mixing seawater into the
460 sediments in $\leq 4\text{m}$ depth.

461 Interestingly, there is a slight positive Li excursion at about 4 m depth in core GC09. This
462 might be related to the mineralogy of this sediment section where the main composition
463 changes from diatomaceous clay to hydrothermal deposit (Fe-rich sulfides; see also Sect.
464 3.3). We suspect that the positive Li anomaly is caused by weak admixing of hydrothermal
465 solutions, as none of the other elements shows drastic concentration changes indicative of
466 early-diagenetic reactions (Gieskes et al., 1982; Chan et al., 1994; Środoń, 1999; Chan and
467 Kastner, 2000; Aloisi et al., 2004; Hensen et al., 2007; Wallmann et al., 2008; Scholz et al.,
468 2009; 2010; 2013). Along with increasing Li concentrations, $^{87}\text{Sr}/^{86}\text{Sr}$ isotope ratios decrease
469 to a value of 0.70908 (Fig.5) and thus tend towards the $^{87}\text{Sr}/^{86}\text{Sr}$ ratio of the local
470 hydrothermal endmember ($^{87}\text{Sr}/^{86}\text{Sr} = 0.7059$; Von Damm, 1990). Hydrothermal endmember
471 Li concentrations in the Guaymas Basin range between 630 and 1076 μM (Von Damm et al.,
472 1985) and are thus 20 to 30 times higher than the Li concentrations measured at the lower
473 end of the core at the Smoker Site ($\sim 34 \mu\text{M}$; Fig. 4, Table S2) indicating a mixing between
474 seawater and hydrothermal fluids with a hydrothermal component of about $\sim 3\%$ (Fig. 7).

475



476



477

478 Fig. 7: NH_4 (µM) (a) and $^{87}\text{Sr}/^{86}\text{Sr}$ ratios (b) versus Li concentrations (µM) of Guaymas Basin
 479 cold seeps (North, Central) and the hydrothermal Smoker vent field. Guaymas deep Smoker
 480 fluids (GC09) mix with hydrothermal fluids with a share of ~3%. For comparison, Guaymas
 481 hydrothermal endmember fluid composition (Von Damm, 1985, 1990), Smoker plume fluid
 482 composition (Berndt et al., 2016), slope sediments (in (a) and deep-sourced cold seeps from
 483 the Gulf of Cadiz (in (a); Hensen et al., 2007)) are shown.

484

485 The hydrothermal activity in the northern trough of the Guaymas Basin can be summarized
 486 to occur only in a relatively confined area affecting the surrounding sediments in a minor
 487 way by lateral heat transfer. The diatomaceous clay might act as a seal to upwards migrating



488 fluids, which are channeled to the catchment area of the rising hydrothermal fluids of the
489 Black Smoker vent field (Fig. 4 in Berndt et al., 2016). The geochemical composition of the
490 upwards migrating hydrothermal fluids is likely influenced by high temperature chemical
491 alteration reactions between the sediment and the intruded sills (Fig. 2b). However,
492 shallower pore fluids of surface sediments at the smoker site (i.e. 0-4 m) are not affected by
493 contributions from these fluids and show predominantly seawater signatures. Despite the
494 elevated heat flow in the vicinity of the hydrothermal vent field, early-diagenetic reactions
495 are also not enhanced as seen e.g. by only slightly elevated NH_4 concentrations and sulfate
496 concentrations that remain at seawater values throughout the cores (Fig. 4).

497

498 4.2.2 Cold seeps

499

500 The selection of sampling sites at presumed seep locations was based on existing published
501 data (Lizarralde et al., 2010) and information from seismic records (see Fig. 2). Seismic
502 amplitude blanking along vertical zones below the seafloor indicates (active?) fluid conduits
503 at North and Central Seep. Following the hypothesis that sill intrusions and related high-
504 temperature alteration of sediments are driving the seepage, the expectation was to find
505 deeply-sourced (average sill depth ~400m) fluids, characterized by a typical geochemical
506 signature analogous to findings at Black Smoker vents in the Guaymas Basin (Von Damm et
507 al., 1985; Berndt et al., 2016). Such characteristics are e.g. a high concentration of
508 thermogenic hydrocarbon gases formed by organic-matter degradation, which is
509 accompanied by enrichments in other organic tracers such as ammonium as well as
510 depletion in Mg and a strong enrichment in fluid-mobile tracers like Li and B (e.g. Aloisi et al.,
511 2004; Scholz et al., 2009).

512 The results from samples obtained using a video-guided MUC show that the highest
513 methane concentrations compared to all other sites were measured at North, Central, and
514 Ring Seeps (Fig. 4b). This and the fact that methane concentrations are exceeding those at
515 the high-accumulation slope station underlines the visual evidence (abundant
516 chemosynthetic biological communities) of active methane seepage. At the two most active
517 sites, North and Central, high methane levels are accompanied by a significant drop in
518 sulfate and increase in alkalinity and H_2S , providing evidence for AOM. These pore water
519 trends are even more pronounced in GC01 (North) where the AOM zone was completely



520 penetrated and gas hydrate was found at about 2.5 mbsf. Unfortunately, GCs from similarly
521 active sites could not be obtained from Central and Ring seeps, mainly because of patchiness
522 of seepage spots and widespread occurrence of authigenic mineralizations at the seafloor
523 preventing sufficient penetration. Nevertheless, the occurrence of active methane seepage
524 at all three investigated sites is evident. A closer look at the lower panel of Fig. 4 a,b (and
525 Table S2) illustrates that the methane flux is not accompanied by any significant excursion of
526 major pore water constituents (e.g. Mg, Cl, Li) that would be typical for deeply-sourced,
527 high-temperature sediment-water interactions. Also Sr concentrations show seawater values
528 throughout all seep sites (Fig. 5), with the exception of North Seep where Sr concentrations
529 in conjunction with Ca (not shown) decrease and point to co-precipitation with Ca during
530 carbonate formation. The $^{87}\text{Sr}/^{86}\text{Sr}$ ratios show predominantly seawater signatures as well
531 (Fig. 5, Table S2). Similarly, NH_4 concentrations, as tracer for the intensity of organic matter
532 decomposition, in both MUCs and GCs, remain at levels $<1\text{mM}$. This is much lower than the
533 end-member reported from vent fluids in the Southern Trough (Von Damm, 1985) and also
534 lower compared to high-accumulation areas like the Slope and the Graben Site (Fig. 4a,b).
535 Essentially, all data presented in Figure 4 show that, with exception of methane and sulfate,
536 the pore water corresponds to ambient diagenetic conditions, typically met in this shallow
537 subsurface depth. An explanation for the decoupling between high methane levels, sulfate
538 depletion at shallow depths, and otherwise more or less unchanged pore water composition
539 is that only methane in form of free gas is rising to the seafloor. This assumption requires a
540 closer look at the composition of dissolved hydrocarbons in general, which is given below.

541

542 4.3 Origin of hydrocarbon gases

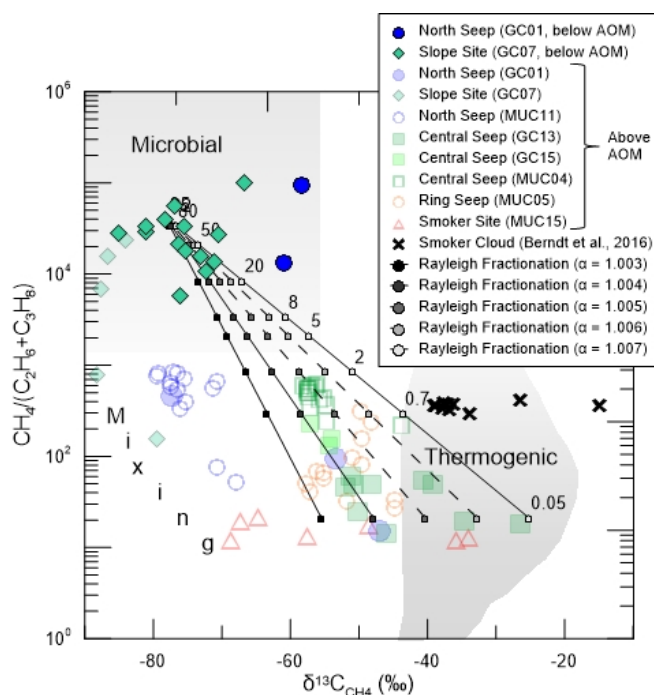
543 4.3.1 Alteration effects

544

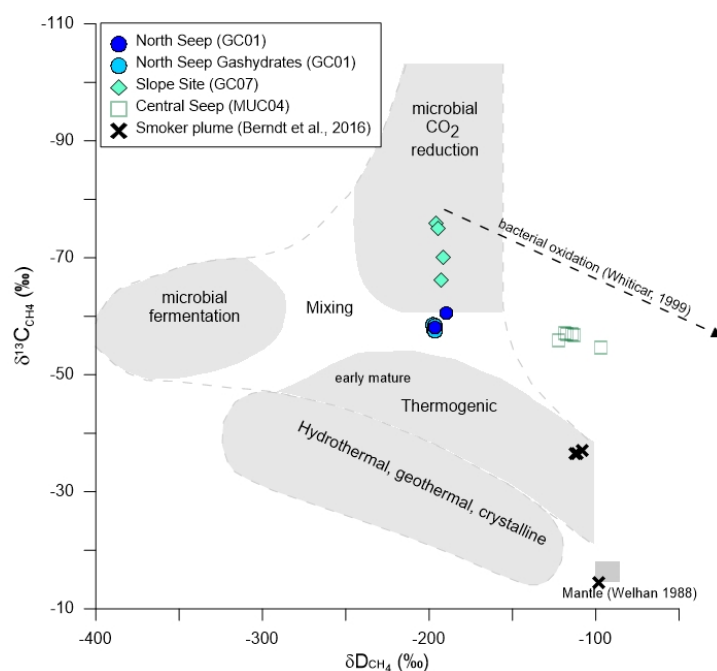
545 The origin of hydrocarbon gases can be deciphered by plotting hydrocarbon $\text{CH}_4/(\text{C}_2\text{H}_6+\text{C}_3\text{H}_8)$
546 ratios versus $\delta^{13}\text{C}_{\text{CH}_4}$ data in a modified Bernard diagram (Schmidt et al., 2005 and literature
547 therein) (Fig. 8) and $\delta^{13}\text{C}_{\text{CH}_4}$ versus $\delta\text{D}_{\text{CH}_4}$ after Whiticar (1999) and Welhan (1988) (Fig. 9).
548 Most of the measured stable isotope data of pore water methane indicate a microbial origin
549 or a mixed microbial and thermogenic origin (Fig. 8, 9). By contrast, the isotopic and
550 geochemical signature of hydrocarbons venting at the Smoker Site reflects a mixture of



551 methane of thermogenic and abiogenic (methane derived from water-rock interactions)
 552 origin (Berndt et al., 2016).
 553



554
 555 Figure 8: Hydrocarbon $\text{CH}_4/(\text{C}_2\text{H}_6+\text{C}_3\text{H}_8)$ ratios versus $\delta^{13}\text{C}_{\text{CH}_4}$ data are shown after a modified
 556 Bernard diagram (Schmidt et al., 2005). Pale symbols indicate samples above the AOM.
 557 Rayleigh fractionation lines show the effect of (microbial) methane oxidation, labels indicate
 558 the residual methane in %.
 559



560

561 Figure 9: Carbon ($\delta^{13}\text{C}_{\text{CH}_4}$) and hydrogen δD isotope data after Whiticar (1999) and (Welhan,
562 1988). Pale symbols (Central Seep (MUC04)) indicate samples above AOM.

563

564 Interestingly, all but two samples from North Seep sediments are located above the AOM
565 (see Fig. 4) and could therefore be affected by oxidation (Fig. 8). Anaerobic methane
566 oxidation enriches CO_2 in ^{12}C which results in a progressively ^{13}C -enriched methane residue
567 shifting the $\delta^{13}\text{C}_{\text{CH}_4}$ values towards heavier values (e.g. Borowski et al., 1997; Dowell et al.,
568 2016). Considering Slope Site methane signatures as a microbial endmember composition
569 for the Guaymas Basin (Fig. 8), most of the data fall on calculated fractionation lines for
570 methane oxidation following a Rayleigh trend (Whiticar et al., 1999). Methane sampled close
571 to the Smoker Site (MUC15) is obviously also affected by anaerobic methane oxidation (Fig.
572 8). This process has recently been described by Dowell et al. (2016), who detected bacterial
573 and archaeal communities in hydrothermal sediments of the southern trough of the
574 Guaymas Basin, which were found to catalyze the oxidation of methane and higher
575 hydrocarbons and shift $\delta^{13}\text{C}_{\text{CH}_4}$ values to heavier signatures.

576 Origin of methane and oxidation effects can further be identified in the $\delta^{13}\text{C}_{\text{CH}_4}$ versus $\delta\text{D}_{\text{CH}_4}$
577 plot after Whiticar (1999) and Welhan (1988) (Fig. 9). Slope Site samples plot in the field of



578 microbial CO₂ reduction while Smoker hydrothermal plume samples plot in the thermogenic
579 field, one sample of the Smoker Site even points to a mantle signature, and thus show clear
580 potential endmember isotope signatures. North Seep samples (pore fluids and gas hydrates)
581 plot in the mixing region while samples from Central Seep clearly shift away from the
582 microbial field and are considered to be affected by bacterial oxidation (Whiticar, 1999).

583 Considering only methane below the AOM as being unaltered, two North Seep samples and
584 the majority of the Slope Site samples show a clear microbial source of methane (Fig. 8). All
585 other samples appear to be affected by high degrees of oxidation following a Rayleigh
586 fractionation process and show that only a fraction between 2 % (MUC 04, Central Seep) and
587 0.05 % (GC15, Central Seep) remains as unoxidized methane (Fig. 8).

588

589 4.3.2 Origin of unaltered samples

590

591 Unaltered North Seep samples show a mixing origin in the $\delta^{13}\text{C}_{\text{CH}_4}$ versus $\delta\text{D}_{\text{CH}_4}$ plot (Fig. 9),
592 possibly stemming from microbial and thermogenic sources. Similar mixing signals of
593 thermogenic and microbial methane have also been observed at Hydrate Ridge (Milkov et
594 al., 2005) and seem to be a common phenomenon in hydrothermal and cold seep affected
595 sediments. In a few samples from North and Central Seep ethane concentrations have been
596 high enough to measure stable carbon isotopes and the $\delta^{13}\text{C}_{\text{C}_2\text{H}_6}$ values point to a
597 thermogenic origin of ethane (Table S3).

598

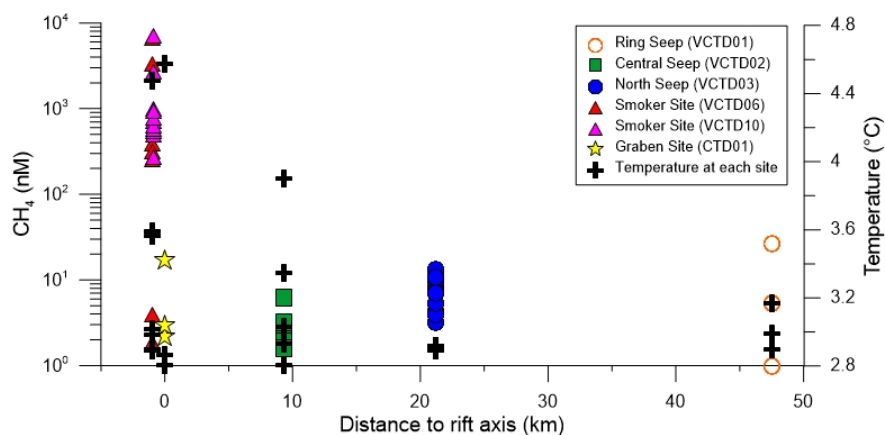
599 4.4 Timing of active (thermogenic) methane release

600

601 Based on the presented data set, even when considering some uncertainties with respect to
602 the fraction of thermogenic methane, the lack of any other geochemical evidence underlines
603 that probably no deep-sourced fluid is migrating upwards at present at the cold seepage
604 sites (compare deep-sourced seepage sites from the Gulf of Cadiz in Fig. 7). Hence, in terms
605 of the original hypothesis that fluid emanation is directly linked to recent sill intrusions, the
606 investigated “cold seep” sites cannot be considered as being active as claimed by Lizarralde
607 et al. (2010), who argue that thermogenic carbon is released up to 50 km away from the rift
608 axis causing a maximum carbon flux of 240 kt C yr⁻¹. First results by Lizarralde et al. (2010)
609 showed temperature anomalies, high methane concentrations, and helium isotopic



610 anomalies indicative of a magmatic source above bright features identified as bacterial mats,
611 tubeworms, and authigenic carbonate. These features are situated above areas of shallow
612 gas above sill intrusions comparable to structures identified in this study by seismic data (Fig.
613 2). The more detailed results of this study regarding pore fluid, water column, and gas
614 geochemistry show that only traces of thermogenic methane were found up to ~20 km off
615 axis (North Seep) and most methane was of microbial origin (Fig. 8, 9). Even pore fluids taken
616 close to the hydrothermal vent area are dominated by shallow microbial degradation
617 processes, indicating that hydrothermal fluid flow in the Guaymas Basin is rather localized
618 and bound to focused fluid pathways. The temperature and chemical anomalies detected by
619 Lizarralde et al. (2010) could also stem from the deep water layer in the Guaymas Basin itself
620 which is influenced by hydrothermal fluids (Campbell and Gieskes, 1984). Hydrothermal
621 activity in the Guaymas Basin produces hydrothermal plumes which rise to 100-300 m above
622 seafloor and then spread out along density gradients throughout the basin (Campbell and
623 Gieskes, 1984). Results of this study show that the Guaymas Basin has a well-mixed bottom
624 seawater layer consisting of patchy and elevated CH_4 , as well as temperatures ranging
625 between 2.8 and 4.5°C in >1000 m depth (Fig. 6 and 10, Table S4). Off-axis methane
626 concentrations vary quite considerably and show e.g. a range from 6 to 28 nM for Ring Seep
627 and a temperature range from 2.8 to 3.9 for Central Seep. These bottom seawater
628 variabilities are bigger than the reported anomalies by Lizarralde et al. (2010) and indicate
629 that their findings might have been overrated.
630



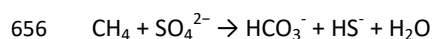
631



632 Fig. 10. Water column CH₄ (colored symbols) and temperature (black crosses) at cold seeps
633 and Smoker/ Graben sites relative to the rift axis.

634

635 Pore fluids taken in a transect from the rift axis up to ~20 km away show no evidence for
636 seepage of fluids that are affected by high-T reactions (Fig. 4). Shallow microbial degradation
637 processes determine pore fluid signatures and control the majority of the released methane
638 (Fig. 4, 8). It is likely the case that high temperature thermogenic reactions acted during sill
639 emplacement and released large amounts of carbon, but these processes appear to have
640 ceased since then. However, pipe structures still may act as high-permeability pathways and
641 facilitate the advection of gas. Small amounts of thermogenic carbon might still be released
642 as seen in microbial and thermogenic mixing signatures of $\delta^{13}\text{C}_{\text{CH}_4}$ and thermogenic $\delta^{13}\text{C}_{\text{C}_2\text{H}_6}$
643 isotope data at North and Central Site. However, present methane advection rates are slow
644 (probably $<1 \text{ cm yr}^{-1}$) as observed by low methane gradients in the pore fluid profiles (Fig. 4).
645 These conditions favor an effective turnover of CH₄ to bicarbonate and authigenic
646 carbonates by AOM (Karaca et al., 2010; Wallmann et al., 2006). The porous authigenic
647 carbonate block recovered from the seafloor at Central Seep can provide long-term
648 information about seepage in this area. The predominant biomarkers found in the seep
649 carbonate from the Central Site (56-VgHG-4) are consistent with an origin from dual species
650 microbial consortia performing the anaerobic oxidation of methane (AOM). High relative
651 abundances of crocetane and *sn*2-hydroxyarchaeol, along with DAGE, indicate major
652 contributions from methanotrophic archaea of the ANME-2 cluster and syntrophic sulfate-
653 reducing bacteria, probably of the *Desulfosarcina–Desulfococcus* group (Blumenberg et al.,
654 2004; Niemann and Elvert, 2008). These consortia appear to gain energy from AOM, with
655 sulfate as the final electron acceptor, according to the net reaction



657 (e.g. Nauhaus et al., 2005; see Wegener et al., 2016 for a recent update).

658 The increase in alkalinity due to the AOM reaction plausibly explains the precipitation of
659 isotopically depleted authigenic carbonates. Particularly, ANME-2 biomarkers have been
660 reported in association with abundant fibrous, often botryoidal aragonite cements
661 (Leefmann et al., 2008), which is fully in line with the observations made at the Central Site
662 (see ch. 3.3). Moreover, the inferred major abundance of ANME-2 indicates that seep



663 carbonate formation once took place under high sulfate concentrations, strong advective
664 methane flow, but no elevated water temperatures (c.f. Nauhaus et al., 2005; Peckmann et
665 al., 2009; Timmers et al., 2015). The observation of minor amounts of typical water column
666 sterols also shows that these seep carbonates do not only carry their inherent AOM
667 signature, but also captured detritus from the surrounding sediment and background water
668 column sources during their ongoing cementation.

669 The bulk carbonate carbon isotope signature ($\delta^{13}\text{C}_{\text{V-PDB}} = -46.6\text{‰}$) overlaps with the shallow
670 heavy $\delta^{13}\text{C}_{\text{CH}_4}$ values (-27.5 and -48.6 ‰) in the pore fluids at Central Seep. Biomarkers found
671 in the bulk carbonate confirm a dominant AOM signature with a significant planktonic and
672 potentially $\delta^{13}\text{C}$ diluting background signal (Fig. S2). The oxygen isotope signature of the bulk
673 carbonate points to a low formation temperature of about 3°C. This is consistent with a
674 formation at ambient seawater which has bottom water temperatures between 2.8 and
675 3.0°C (Fig. 6, 10; Table S4). The $^{87}\text{Sr}/^{86}\text{Sr}$ analyses support this assumption by values within
676 uncertainty identical to modern seawater. Also U-Th carbonate dating performed at these
677 authigenic carbonates provide formation ages younger than 240 yrs BP. In conclusion,
678 authigenic carbonate shows a recent to sub-recent formation age with methane from
679 shallow sources at ambient seawater and thus confirms the results from pore fluid and gas
680 geochemistry of cessation of deep fluid and gas mobilization.

681 Taking a closer look at the seismic lines across the seep locations, it becomes obvious that
682 the disrupted sediment layers are not reaching to the sediment surface (Fig. 2a, c). This
683 implies that fluid mobilization ceased at some time before the uppermost sediment layers
684 were deposited. The doming above the Central Seep provides some clues on the timing of
685 fluid migration (Fig. 2c). Assuming that the doming is the result of buoyancy-related uplift
686 (Koch et al., 2015) it represents the time when intrusion-related gas reached the sea floor.
687 Assuming further a sedimentation rate of 1.7 m per 1000 years (Central Seep; Table 1) and
688 maxima and minima deposition depths of 48 and 12 m respectively below seafloor (see Fig.
689 2c) this would imply that most of the gas reached the seafloor between 28 and 7 kyrs ago.
690 Even assuming minima and maxima sedimentation rates of 3.5 m (North Seep) and 0.5 m
691 (Ring Seep) per 1000 years gas flow would have ceased at the earliest between 14 and 3 kyrs
692 ago or at the latest 96 and 24 kyrs ago. This finding supports the results of the pore fluid and



693 gas geochemistry which show no sign of active fluid flow from depth at cold seep sites in the
694 northern Guaymas Basin.

695 Large amounts of CH₄ (and CO₂) must have been emitted to bottom waters during the
696 calculated periods (s.a.), rapidly after sills intruded into the organic-rich sediments in the
697 Guaymas Basin. However, these carbon emissions must have ceased after sill-emplacment
698 ended and the impact on climate appears to depend on the durability of the magmatic
699 system.

700

701 **5 Conclusions**

702

703 Magmatic intrusions into organic-rich sediments can potentially release large amounts of
704 carbon into the water column and atmosphere and are therefore discussed as potential
705 trigger mechanisms for rapid climate change, e.g. during the PETM. In the Guaymas Basin,
706 off-axis cold seeps do not show indications for present-day hydrothermal activity. Pore fluids
707 sampled from cold seep structures and in the vicinity of hydrothermal vents in the northern
708 Guaymas Basin, are dominated by seawater concentrations and show no sign of deep fluids
709 or temperature-related diagenesis. Methane measured at the investigated sites stems from
710 a mixed origin (microbial and thermogenic sources), though mainly from microbial
711 processes. This may suggest that hydrothermal circulation has stopped at depth and, based
712 on seismic data, ceased more than 7kyrs ago. Sill-induced hydrothermal systems appear to
713 be an effective way to release carbon, but the period of time depends on the longevity of
714 the magmatic system.

715

716 **Acknowledgments**

717

718 This work was undertaken within the MAKS project which was funded by the German
719 Ministry of Science and Education (BMBF). We would like to thank the master and crew of
720 the R/V Sonne for their help and support during the SO241 cruise. Further thanks goes to
721 Regina Surberg, Bettina Domeyer, and Anke Bleyer for analytical support during the cruise
722 and on shore. We greatly appreciate the support from Ana Kolevica, Tyler Goepfert,
723 Sebastian Fessler, Andrea Bodenbinder, Yan Shen, and Jutta Heinze for onshore analyses.

724

725 **References**

- 726 Aloisi, G., Drews, M., Wallmann, K. and Bohrmann, G.: Fluid expulsion from the Dvurechenskii mud
727 volcano (Black Sea). Part I. Fluid sources and relevance to Li, B, Sr, I and dissolved inorganic nitrogen
728 cycles, *Earth Planet. Sci. Lett.*, 225(3–4), 347–363, doi:10.1016/j.epsl.2004.07.006, 2004.
- 729 Berndt, C., Hensen, C., Mortera-Gutierrez, C., Sarkar, S., Geilert, S., Schmidt, M., Liebetrau, V., Kipfer,
730 R., Scholz, F., Doll, M., Muff, S., Karstens, J., Planke, S., Petersen, S., Böttner, C., Chi, W.-C., Moser, M.,
731 Behrendt, R., Fiskal, A., Lever, M. A., Su, C.-C., Deng, L., Brennwald, M. S. and Lizarralde, D.: Rifting
732 under steam – how rift magmatism triggers methane venting from sedimentary basins, *Geology*,
733 44(9), 767–770, 2016.
- 734 Biddle, J. F., Cardman, Z., Mendlovitz, H., Albert, D. B., Lloyd, K. G., Boetius, A. and Teske, A.:
735 Anaerobic oxidation of methane at different temperature regimes in Guaymas Basin hydrothermal
736 sediments, *ISME J.*, 6(5), 1018–1031, doi:10.1038/ismej.2011.164, 2012.
- 737 Blumenberg, M., Seifert, R., Reitner, J., Pape, T. and Michaelis, W.: Membrane lipid patterns typify
738 distinct anaerobic methanotrophic consortia, *Proc. Natl. Acad. Sci. USA*, 101, 11111–11116, 2004.
- 739 Borowski, W. S., Paull, C. K. and Ussler III, W.: Carbon cycling within the upper methanogenic zone of
740 continental rise sediments: An example from the methane-rich sediments overlying the Blake Ridge
741 gas hydrate deposits, *Mar. Chem.*, 57, 299–311, 1997.
- 742 Brumsack, H. J. and Gieskes, J. M.: INTERSTITIAL WATER TRACE-METAL CHEMISTRY OF LAMINATED
743 SEDIMENTS FROM THE GULF OF CALIFORNIA, MEXICO, *Mar. Chem.*, 14, 89–106, 1983.
- 744 Calvert, S. E.: Accumulation of Diatomaceous Silica in the Sediments of the Gulf of California, *Geol.*
745 *Soc. Am. Bull.*, 77(June), 569–596, 1966.
- 746 Campbell, A. C. and Gieskes, J. M.: Water column anomalies associated with hydrothermal activity in
747 the Guaymas Basin, Gulf of California Andrew C. Campbell and Joris M. Gieskes, *Earth Planet. Sci.*
748 *Lett.*, 68, 57–72, 1984.
- 749 Chan, L. H., Gieskes, J. M., You, C. F. and Edmond, J. M.: Lithium Isotope Geochemistry of Sediments
750 and Hydrothermal Fluids of the Guaymas Basin, Gulf of California, *Geochim. Cosmochim. Acta*,
751 58(20), 4443–4454 [online] Available from: //a1994pp04300015, 1994.
- 752 Curray, J. R. and Moore, D. G. et al.: Initial Reports of the Deep Sea Drilling Project. vol. 64., U.S.
753 Govt. Printing Office, Washington., 1982.
- 754 Von Damm, K. L., Edmond, J. M., Measures, C. I. and Grant, B.: Chemistry of submarine hydrothermal
755 solutions at Guaymas Basin, Gulf of California, *Geochim. Cosmochim. Acta*, 49(11), 2221–2237, 1985.
- 756 Von Damm, K.: Seafloor Hydrothermal Activity: Black Smoker Chemistry And Chimneys, *Annu. Rev.*
757 *Earth Planet. Sci.*, 18(1), 173–204, doi:10.1146/annurev.earth.18.1.173, 1990.
- 758 DeMaster, D.: The supply and accumulation of silica in the marine environment, *Geochim.*
759 *Cosmochimica Acta*, 5, 1715–1732, 1981.
- 760 Dickens, G. R.: Rethinking the global carbon cycle with a large, dynamic and microbially mediated gas
761 hydrate capacitor, *Earth Planet. Sci. Lett.*, 213(3–4), 169–183, doi:10.1016/S0012-821X(03)00325-X,
762 2003.
- 763 Dowell, F., Cardman, Z., Dasarathy, S., Kellermann, M. Y., Lipp, J. S., Ruff, S. E., Biddle, J. F., McKay, L.
764 J., MacGregor, B. J., Lloyd, K. G., Albert, D. B., Mendlovitz, H., Hinrichs, K. U. and Teske, A.: Microbial
765 communities in methane- and short chain alkane-rich hydrothermal sediments of Guaymas Basin,



- 766 Front. Microbiol., 7(JAN), doi:10.3389/fmicb.2016.00017, 2016.
- 767 Einsele, G., Gieskes, J. M., Curray, J., Moore, D. M., Aguayo, E., Aubry, M.-P., Fornari, D., Guerrero, J.,
768 Kastner, M., Kelts, K., Lyle, M., Matoba, Y., Molina-Cruz, A., Niemitz, J., Rueda, J., Saunders, A.,
769 Schrader, H., Simoneit, B. and Vacquier, V.: Intrusion of basaltic sills into highly porous sediments,
770 and resulting hydrothermal activity, *Nature*, 283, 441–445, doi:10.1017/CBO9781107415324.004,
771 1980.
- 772 Fisher, A. T. and Becker, K.: Heat flow, hydrothermal circulation and basalt intrusions in the Guaymas
773 Basin, Gulf of California, *Earth Planet. Sci. Lett.*, 103(1–4), 84–99, doi:10.1016/0012-821X(91)90152-
774 8, 1991.
- 775 Gieskes, J. M., Kastner, M., Einsele, G., Kelts, K. and Niemitz, J.: Hydrothermal Activity in the Guaymas
776 Basin, Gulf of California: A synthesis, in *In Initial Reports of the Deep Sea Drilling Project. vol. 64, Pt.*
777 *2*, edited by D. G. et al. Curray, J.R., Moore, pp. 1159–1167., 1982.
- 778 Gieskes, J. M., Gamo, T. and Brumsack, H.: Chemical methods for interstitial water analysis aboard
779 Joides Resolution, *Ocean Drill. Prog. Tech. Note 15*. Texas A&M Univ. Coll. Stn., 1991.
- 780 Gutjahr, M., Ridgwell, A., Sexton, P. F., Anagnostou, E., Pearson, P. N., Pälike, H., Norris, R. D.,
781 Thomas, E. and Foster, G. L.: Very large release of mostly volcanic carbon during the Palaeocene–
782 Eocene Thermal Maximum, *Nature*, 548(7669), 573–577, doi:10.1038/nature23646, 2017.
- 783 Hartmann, A. and Villinger, H.: Inversion of marine heat flow measurements by expansion of the
784 temperature decay function, *Geophys. J. Int.*, 148(3), 628–636, doi:10.1046/j.1365-
785 246X.2002.01600.x, 2002.
- 786 Henry, P., Le Pichon, X., Lallement, S., Lance, S., Martin, J. B., Foucher, J. P., Fiala-Médioni, A., Rostek,
787 F., Guilhaumou, N., Pranal, V. and Castrec, M.: Fluid flow in and around a mud volcano seaward of
788 the Barbados accretionary wedge: Results from Manon cruise, *J. Geophys. Res.*, 101(9), 20297–
789 20323, 1996.
- 790 Hensen, C., Nuzzo, M., Hornibrook, E., Pinheiro, L. M., Bock, B., Magalhães, V. H. and Brückmann, W.:
791 Sources of mud volcano fluids in the Gulf of Cadiz-indications for hydrothermal imprint, *Geochim.*
792 *Cosmochim. Acta*, 71(5), 1232–1248, doi:10.1016/j.gca.2006.11.022, 2007.
- 793 Howarth, R. J. and McArthur, J. M.: Strontium isotope stratigraphy, in *A Geological Time Scale, with*
794 *Look-up Table Version 4*, edited by F. M. Gradstein and J. G. Ogg, pp. 96–105, Cambridge University
795 Press, Cambridge, U.K pp. ., 2004.
- 796 Huh, C.-A., Su, C.-C., Wang, C.-H., Lee, S.-Y. and Lin, I.-T.: Sedimentation in the Southern Okinawa
797 Trough – Rates, turbidites and a sediment budget, *Mar. Geol.*, 231, 129–139, 2006.
- 798 Karaca, D., Hensen, C. and Wallmann, K.: Controls on authigenic carbonate precipitation at cold seeps
799 along the convergent margin off Costa Rica, *Geochemistry, Geophys. Geosystems*, 11(8), 1–19,
800 doi:10.1029/2010GC003062, 2010.
- 801 Kastner, M.: Evidence for Two Distinct Hydrothermal Systems in the Guaymas Basin, in *In Initial*
802 *Reports of the Deep Sea Drilling Project. vol. 64, Pt. 2*, edited by D. G. et al. Curray, J.R., Moore, pp.
803 1143–1157, U.S. Govt. Printing Office, Washington., 1982.
- 804 Kastner, M. and Siever, R.: Siliceous Sediments of the Guaymas Basin: The Effect of High Thermal
805 Gradients on Diagenesis, *J. Geol.*, 91(6), 629–641, doi:10.1086/628816, 1983.
- 806 Kennett, J. P., Cannariato, K. G., Hendy, I. L. and Behl, R. J.: Carbon Isotopic Evidence for Methane
807 Hydrate Instability During Quaternary Interstadials, *Science* (80-.), 288(5463), 128–133,



- 808 doi:10.1126/science.288.5463.128, 2000.
- 809 Koch, S., Berndt, C., Bialas, J., Haeckel, M., Crutchley, G., Papenberg, C., Klaeschen, D. and Greinert,
810 J.: Gas-controlled seafloor doming, *Geology*, 43(7), 571–574, doi:doi: 10.1130/G36596.1, 2015.
- 811 Lee, S.-Y., Huh, C.-A., Su, C.-C. and You, C.-F.: Sedimentation in the Southern Okinawa Trough:
812 enhanced particle scavenging and teleconnection between the Equatorial Pacific and western Pacific
813 margins, *Deep. Res.*, 51, 1769–1780, 2004.
- 814 Leefmann, T., Bauermeister, J., Kronz, A., Liebetrau, V., Reitner, J. and Thiel, V.: Miniaturized
815 biosignature analysis reveals implications for the formation of cold seep carbonates at Hydrate Ridge
816 (off Oregon, USA), *Biogeosciences*, 5, 731–738, 2008.
- 817 Lizarralde, D., Soule, S. A., Seewald, J. S. and Proskurowski, G.: Carbon release by off-axis magmatism
818 in a young sedimented spreading centre, *Nat. Geosci.*, 4(1), 50–54, doi:10.1038/ngeo1006, 2010.
- 819 Lonsdale, P. and Becker, K.: Hydrothermal plumes, hot springs, and conductive heat flow in the
820 Southern Trough of Guaymas Basin, *Earth Planet. Sci. Lett.*, 73(2–4), 211–225, doi:10.1016/0012-
821 821X(85)90070-6, 1985.
- 822 Lupton, J. E.: Helium-3 in the Guaymas Basin: Evidence for injection of mantle volatiles in the Gulf of
823 California, *J. Geophys. Res.*, 84(B13), 7446, doi:10.1029/JB084iB13p07446, 1979.
- 824 Milkov, A. V., Claypool, G. E., Lee, Y. J. and Sassen, R.: Gas hydrate systems at Hydrate Ridge offshore
825 Oregon inferred from molecular and isotopic properties of hydrate-bound and void gases, *Geochim.*
826 *Cosmochim. Acta*, 69(4), 1007–1026, doi:10.1016/j.gca.2004.08.021, 2005.
- 827 Nauhaus, K., Treude, T., Boetius, A. and Krüger, M.: Environmental regulation of the anaerobic
828 oxidation of methane: A comparison of ANME-I and ANME-II communities, *Environ. Microbiol.*, 7, 98–
829 106, 2005.
- 830 Niemann, H. and Elvert, M.: Diagnostic lipid biomarker and stable isotope signatures of microbial
831 communities mediating the anaerobic oxidation of methane with sulphate, *Org. Geochem.*, 39,
832 1668–1677, 2008.
- 833 Peckmann, J., Birgel, D. and Kiel, S.: Molecular fossils reveal fluid composition and flow intensity at a
834 Cretaceous seep, *Geology*, 37, 847–850, 2009.
- 835 Pfender, M. and Villinger, H.: Miniaturized data loggers for deep sea sediment temperature gradient
836 measurements, *Mar. Geol.*, 186(3–4), 557–570, doi:10.1016/S0025-3227(02)00213-X, 2002.
- 837 Schmidt, M., Hensen, C., Mörz, T., Müller, C., Grevemeyer, I., Wallmann, K., Mau, S. and Kaul, N.:
838 Methane hydrate accumulation in “Mound 11” mud volcano, Costa Rica forearc, *Mar. Geol.*, 216(1–
839 2), 83–100, doi:10.1016/j.margeo.2005.01.001, 2005.
- 840 Schmidt, M., Sommer, S. and Esser, D.: Natural CO₂ Seeps Offshore Panarea ; , 49(1), 19–30, 2015.
- 841 Scholz, F., Hensen, C., Reitz, A., Romer, R. L., Liebetrau, V., Meixner, A., Weise, S. M. and Haeckel, M.:
842 Isotopic evidence (⁸⁷Sr/⁸⁶Sr, ^δ7Li) for alteration of the oceanic crust at deep-rooted mud volcanoes
843 in the Gulf of Cadiz, NE Atlantic Ocean, *Geochim. Cosmochim. Acta*, 73(18), 5444–5459,
844 doi:10.1016/j.gca.2009.06.004, 2009.
- 845 Scholz, F., Hensen, C., De Lange, G. J., Haeckel, M., Liebetrau, V., Meixner, A., Reitz, A. and Romer, R.
846 L.: Lithium isotope geochemistry of marine pore waters - Insights from cold seep fluids, *Geochim.*
847 *Cosmochim. Acta*, 74(12), 3459–3475, doi:10.1016/j.gca.2010.03.026, 2010.



- 848 Scholz, F., Hensen, C., Schmidt, M. and Geersen, J.: Submarine weathering of silicate minerals and the
849 extent of pore water freshening at active continental margins, *Geochim. Cosmochim. Acta*, 100, 200–
850 216, doi:10.1016/j.gca.2012.09.043, 2013.
- 851 Simoneit, B. R. T., Summerhayes, C. P. and Meyers, P. A.: Sources and Hydrothermal Alteration of
852 Organic-Matter in Quaternary Sediments - a Synthesis of Studies from the Central Gulf of California,
853 *Mar. Pet. Geol.*, 3(4), 282–297, 1986.
- 854 Simoneit, B. R. T., Leif, R. N., Sturz, A. A., Sturdivant, A. E. and Gieskes, J. M.: Geochemistry of shallow
855 sediments in Guaymas Basin, gulf of California: hydrothermal gas and oil migration and effects of
856 mineralogy, *Org. Geochem.*, 18(6), 765–784, doi:10.1016/0146-6380(92)90046-Z, 1992.
- 857 Sommer, S., Linke, P., Pfannkuche, O., Schleicher, T., Deimling, J. S. V., Reitz, A., Haeckel, M., Flögel,
858 S. and Hensen, C.: Seabed methane emissions and the habitat of frenulate tubeworms on the Captain
859 Arutyunov mud volcano (Gulf of Cadiz), *Mar. Ecol. Prog. Ser.*, 382, 69–86, doi:10.3354/meps07956,
860 2009.
- 861 Środoń, J.: Nature of Mixed-Layer Clays and Mechanisms of Their Formation and Alteration, *Annu.*
862 *Rev. Earth Planet. Sci.*, 27(1), 19–53, doi:10.1146/annurev.earth.27.1.19, 1999.
- 863 Svensen, H., Planke, S., Malthes-Sorensen, A., Jamtveit, B., Myklebust, R., Eidem, T. R. and Rey, S. S.:
864 Release of methane from a volcanic basin as a mechanism for initial Eocene global warming, *Nature*,
865 429(June), 3–6, doi:10.1038/nature02575.1., 2004.
- 866 Teske, A., Callaghan, A. V. and LaRowe, D. E.: Biosphere frontiers of subsurface life in the sedimented
867 hydrothermal system of Guaymas Basin, *Front. Microbiol.*, 5(JULY), 1–11,
868 doi:10.3389/fmicb.2014.00362, 2014.
- 869 Teske, A., De Beer, D., McKay, L. J., Tivey, M. K., Biddle, J. F., Hoer, D., Lloyd, K. G., Lever, M. A., Røy,
870 H., Albert, D. B., Mendlovitz, H. P. and MacGregor, B. J.: The Guaymas Basin hiking guide to
871 hydrothermal mounds, chimneys, and microbial mats: Complex seafloor expressions of subsurface
872 hydrothermal circulation, *Front. Microbiol.*, 7(FEB), 1–23, doi:10.3389/fmicb.2016.00075, 2016.
- 873 Timmers, P. H., Widjaja-Greefkes, H.A. Ramiro-Garcia, J., Plugge, C. M. and Stams, A. J.: Growth and
874 activity of ANME clades with different sulfate and sulfide concentrations in the presence of methane,
875 *Front. Microbiol.*, 6, 988, 2015.
- 876 Wallmann, K., Drews, M., Aloisi, G. and Bohrmann, G.: Methane discharge into the Black Sea and the
877 global ocean via fluid flow through submarine mud volcanoes, *Earth Planet. Sci. Lett.*, 248(1–2), 544–
878 559, doi:10.1016/j.epsl.2006.06.026, 2006.
- 879 Wegener, G., Krukenberg, V., Ruff, S. E., Kellermann, M. Y. and Knittel, K.: Metabolic capabilities of
880 microorganisms involved in and associated with the anaerobic oxidation of methane, *Front.*
881 *Microbiol.*, 7, 46, 2016.
- 882 Welhan, J. A.: Origins of methane in hydrothermal systems, *Chem. Geol.*, 71(1–3), 183–198,
883 doi:10.1016/0009-2541(88)90114-3, 1988.
- 884 Whiticar, M. J.: Carbon and hydrogen isotope systematics of bacterial formation and oxidation of
885 methane, , 161, 291–314, 1999.
- 886 Zachos, J. C., Wara, M. W., Bohaty, S., Delaney, M. L., Petrizzo, M. R., Brill, A., Bralower, T. J. and
887 Premoli-Silva, I.: A transient rise in tropical sea surface temperature during the Paleocene-Eocene
888 thermal maximum., *Science*, 302(5650), 1551–1554, doi:10.1126/science.1090110, 2003.
- 889



Table 1: Station list and site names of GCs and MUCs taken in the Guaymas Basin with according water depth. Heat flow and temperature gradient data measured either attached to GCs or to a sediment probe.

Site	Site name	Latitude (N)	Longitude (W)	Water depth (m)	Temp. gradient (K/m)	Heat flow (mW/m ²)	Sed. rate (m/kyr)	Mass acc. rate (g/cm ² /yr)
Gravity corer								
St.07 - GC01	North Seep Reference	27°33.301'	111°32.882'	1845	0.14	28	-	-
St.10 - GC04	Site Central	27°26.531'	111°29.928'	1846	0.22	140	-	-
St.09 - GC03	Seep Central	27°28.138'	111°28.420'	1837	-	-	-	-
St.09 - GC13	Seep Central	27°28.193'	111°28.365'	1838	0.16	113	-	-
St.72 - GC15	Seep Smoker	27°28.178'	111°28.396'	1837	-	-	-	-
St.51 - GC09	Site Smoker	27°24.472'	111°23.377'	1840	11	8069	-	-
St.58 - GC10	Site	27°24.478'	111°23.377'	1845	10	6509	-	-
St.47 - GC07	Slope Site	27°24.412'	111°13.649'	671	-	-	-	-
Multicorer								
St.33 - MUC11	North Seep	27° 33.301'	111° 32.883'	1855	-	-	1.7* 3.5 [#]	0.05* 0.15 [#]
St.23 - MUC05	Ring Seep	27° 30.282'	111° 40.770'	1726	-	-	0.5	0.01
St.15 - MUC02	Reference Site	27°26.925'	111°29.926'	1845	-	-	2.3	0.04
St.22 - MUC04	Central Seep	27° 28.165'	111° 28.347'	1839	-	-	1.7	0.04
St.65 - MUC15	Smoker Site	27° 24.577'	111° 23.265'	1846	-	-	1.8	0.05
St.66 - MUC16	Smoker Site	27° 24.577'	111° 23.265'	1842	-	-	2.1' 0.4 [†]	0.08' 0.02 [†]
St29 - MUC09	Slope Site	27°42.410'	111°13.656'	665	-	-	-	-
HF lance								
St.60a - HF008_P03		27°24.273'	111°23.396'	1840	4.6	3206	-	-
St.60a - HF008_P01		27°24.623'	111°23.626'	1834	0.86	599	-	-
St.60a - HF008_P02	Smoker Site	27°24.554'	111°23.512'	1840	2.8	1953	-	-
St.60a - HF008_P04		27°24.408'	111°23.288'	1849	2039	1427	-	-
St.60a - HF008_P05		27°24.341'	111°23.177'	1852	1014	710	-	-
St.60a - HF008_P06		27°24.265'	111°23.082'	1844	0.74	516	-	-



St.60b -								
HF008_P07		27°24.193'	111°23.956'	1834	0.8	579	-	-
St.60b -								
HF009_P04		27°24.543'	111°23.351'	1837	15	10835	-	-
St.60b -								
HF009_P01		27°24.605'	111°23.317'	1837	0.39	274	-	-
St.60b -								
HF009_P02		27°24.552'	111°23.347'	1834	3451	2415	-	-
St.70 -								
HF011_P01		27°25.802'	111°25.486'	1870	0.38	262	-	-
St.70 -								
HF011_P02	Graben	27°25.460'	111°24.946'	2019	0.48	338	-	-
St.70 -	Site							
HF011_P03		27°25.955'	111°24.493'	2046	0.43	302	-	-
St.70 -								
HF011_P04		27°25.837'	111°24.951'	2025	0.46	320	-	-
Authigenic carbonate								
St.56-	Central							
VgHG-4	Seep	27°28.181'	111°28.379'	1843	-	-	-	-

*#Sedimentation and mass accumulation rates at Station 33 of the 0-13 cm, 13-18 cm layers, respectively

^Sedimentation and mass accumulation rates at Station 65 of the 0 - 7 cm, 7 - 17 cm layers, respectively